A versatile tiling light sheet microscope for cleared tissue imaging

Xiaoliang Li[1,2,3,10], Dongdong Zhang[1,2,10], Chunhui Wang[1,2,10], Xuzhao Li [1,2], Mengjie Lai[3], Yao Weng[3], Ruili Feng[4], Xinyi Shirley Zhang[5], Yanlu Chen[1,2], Jing Yu[3], Dongyue Wang[1,2], Rui Nie[1,2], Xiao Yang[6], Yongyi Chen[7], Bi-Chang Chen[8], Yi Feng[9], Bo Zhou[5], Shang Cai[1,2,*], Jie-Min Jia[1,2,*], Liang Gao[1,2,*]

1. School of Life Sciences, Westlake University, Hangzhou, Zhejiang Province, 310024, China.

2. Institute of Basic Medical Sciences, Westlake Institute for Advanced Study, Hangzhou, Zhejiang Province, 310024, China.

3. Nuohai Life Science Co.,Ltd, Shanghai, 201619, China.

4. Laboratory of Molecular Neural Biology, School of Life Sciences, Shanghai University, Shanghai 200444, China.

5. State Key Laboratory of Cell Biology, Shanghai Institute of Biochemistry and Cell Biology, Chinese Academy of Sciences, University of Chinese Academy of Sciences, Shanghai, 200031, China.

6. State Key Laboratory of Proteomics, Beijing Proteome Research Center, National Center for Protein Sciences, Beijing Institute of Lifeomics, Beijing, 102206, China

7. Department of Clinical laboratory, Zhejiang Cancer Hospital, Hangzhou, Zhejiang Province, 310000, China.

8. Research Center for Applied Sciences, Academia Sinica, Taipei, 11529, Taiwan.

9. Department of Integrative Medicine and Neurobiology, School of Basic Medical Sciences, Fudan University, Shanghai, 200032, China.

10. These authors contributed equally to this work.

*Correspondence: gaoliang@westlake.edu.cn; jiajiemin@westlake.edu.cn; caishang@westlake.edu.cn

Abstract

We present a versatile tiling light sheet microscope with advanced multicolor 3D imaging ability to image cleared tissues rapidly at cellular to subcellular spatial resolutions. The microscope is capable to adjust the spatial resolution and imaging speed conveniently based on needs, and it aligns semi-automatically to ensure the optimal imaging result regardless the imaging conditions and user skills. We demonstrate the microscope by imaging mouse organs and human tissue cleared by different methods.

High resolution 3D fluorescence imaging of biological tissues bridges the observation and understanding of organisms at cellular and tissue level. Imaging physically sectioned tissue slices has been the only way to perform the study [1-4]. Tissue clearing enables the use of advanced 3D fluorescence imaging techniques to acquire tissue structure information much more efficiently [5-11], and light sheet microscopy (LSM) was hereby recruited [12-17]. Unfortunately, cleared tissue imaging with LSM is still in development, and it is challenging to implement the technique in different researches because of problems caused by both LSM and tissue clearing methods.

Conventional LSM is inefficient in cleared tissue imaging. Usually, a large cleared tissue specimen is imaged with LSM by collecting multiple 3D image stacks from subdivided sample volumes sequentially. The 3D image of the whole specimen is obtained by registering and merging the acquired 3D image stacks (Supplementary Fig. 1). The strategy works, but it is problematic due to the inherited tradeoff between the spatial resolution and the size of the field of view (FOV) in LSM. The spatial resolution is higher with smaller subdivided sample volumes, i.e. the size of the FOV, as thinner light sheets and higher detection numerical apertures (NA) can be used to image. However, the time and effort spent on image acquisition and image reconstruction increase massively as the FOV becomes smaller [18]. Conversely, the spatial resolution and the optical sectioning ability of LSM drop quickly as the size of the FOV and light sheet thickness increase. Thus, a major challenge of improving LSM for cleared tissue imaging is to achieve the desired spatial resolution while reducing the suffering caused by the time-consuming image acquisition and reconstruction process.

Tissue clearing methods also cause significant limitations. Different clearing methods are suited for different types of tissues. Tissues cleared by different methods have different clarity, optical refractive indexes, mechanical strengths, chemical properties, and morphological distortions, which result in different limitations on sample labeling, handling, and imaging methods. The evaluation, improvement, and development of tissue fixation, clearing, and labeling methods are unsettled and progressing aggressively, and it is difficult to predict the ultimate functionalities and properties of the tissue clearing technique. A versatile microscope

that fits various types of tissues cleared and labeled by different methods is therefore essential to facilitate the application and improvement of the tissue clearing and related techniques.

Despite the attention received by cleared tissue imaging with LSM and the technical advances to be expected, more significant values and potentials of the combination are yet to be discovered. Therefore, lower the threshold to adopt cleared tissue imaging with LSM in different researches and enable the participation of more scientists with different backgrounds are critical to accelerate the progress.

To fulfill our vision, we developed a tiling light sheet microscope for cleared tissue imaging (Supplementary Fig. 2-5) [19]. Besides having a more advanced multicolor 3D imaging ability than that of conventional light sheet microscopes, the ability to image biological tissues of centimeter sizes, cleared by different methods, at micron level spatial resolutions rapidly in minutes to hours, the microscope also focuses on a feasible and balanced performance. Altogether, we deliver an advanced, flexible, reliable, widely applicable, and easily adoptable microscope for cleared tissue imaging (Fig. 1a).

Our microscope has several unique features. Tiling light sheets are used to image samples at high spatial resolution more efficiently than conventional LSM (Supplementary Fig. 1). Both the detection magnification and the excitation light sheet can be adjusted easily to image samples at different spatial resolutions and imaging speeds base on needs (Supplementary Fig. 6,7). Illumination light phase modulation through the spatial light modulator (SLM) in the microscope is used to overcome almost all alignment problems (Supplementary Fig. 8,9), which also enables semi-automatic alignment of our microscope and makes it extremely stable, reliable, easy to operate and maintain.

We evaluated the microscope and compared it with a Zeiss Z1 light sheet microscope. A PEGASOS cleared Thy1/YFP mouse brain was first imaged with the Z1 in 1.5 hours [20]. Next, the sample was transferred to our microscope and imaged in a high resolution mode and a high speed mode in 5 hours and 12 minutes respectively. A 50 ms camera exposure time was used in all experiments. A more informative result was obtained with the high resolution mode of our microscope at a spatial resolution of ~2 by 2 by 5 μm^3 (Fig. 1), compared to an estimated ~2 by 2 by 15 μm^3 spatial resolution obtained with the Z1. The sample was also examined much faster

with our microscope despite at a lower spatial resolution of ~4 by 4 by 10 μm^3 (Supplementary Fig. 10-14, Supplementary Video 1). The axial resolution of the high speed mode result is still better than that of the Z1 because our microscope is capable to adjust the lateral position of the excitation light sheet. So that the shortest and thinnest light sheet can be centered on the specimen and used to image. Indeed, the ability to adjust the geometry and position of the excitation light sheet in cleared tissue imaging with LSM is not only favored but also required (Supplementary Fig. 15). It is worth of mentioning that the advances of using tiling light sheets would be more significant by using cameras with more pixels (Supplementary Fig. 1).

The use of long working distance air objectives makes our microscope easy to operate and compatible with different clearing methods without being contaminated or damaged by the imaging buffer. It also reduces the instrument cost and maintenance requirements significantly. Different mounting methods are used to mount tissues of different types, sizes, shapes, and mechanical strengths (Fig. 2a-f, Supplementary Fig. 3,4,14-20, Supplementary Video 2). Additionally, the illumination, detection, imaging chamber, and sample translation subsystems of our microscope are all independent, so that each subsystem can be modified individually to fit applications beyond the imaging ability of the current design. Submicron spatial resolution and live imaging ability are obtained with nearly identical design but different excitation objectives, detection objectives, imaging chambers, and translational stages (Fig. 2g-l, Supplementary Fig. 22-24, Supplementary Video 3).

The desired spatial resolution should be chosen carefully regardless the imaging ability. Tissue fixation and clearing introduce morphological distortions. The distortions should be smaller than the spatial resolution to make the imaging meaningful [21, 22]. The amount of data is overwhelming, and it increases cubically with the spatial resolution. Petabytes of data are common in researches involving 3D imaging of a large number of cleared samples, which are difficult to manage and process with conventional data analysis workflows. With the flexibility and the semi-automatic alignment ability of our microscope, users have the freedom to control the imaging and data collection process, by which the best imaging strategy can be practiced.

Our microscope enables detailed observations of complicated tissue structures. The entire mouse brain vessel network was revealed with nearly every capillary (Fig. 2m-cc, Supplementary Video 4-6). Our result for the first time shows that the first level of penetrating vessels in the cerebral cortex is directly connected to the same level of vessels in the hippocampus at the corpus callosum. The more advanced 3D imaging ability of our microscope would certainly facilitate studies to understand the vessel network in the brain (Fig. 2p-u), which have been hindered due to the lack of efficient methods to assess the vessel network in whole brains precisely.

The alignment of different color channels is ensured in our microscope (Supplementary Fig. 8,9), by which the relationship between different tissue structures can be determined accurately with multicolor imaging. We imaged a mouse mammary gland immuno-stained with Krt14/AF488, a mammary basal cell marker, and Cd200/AF594, expressed in endothelial, stromal, and part of luminal cells, and cleared with Adipo-clear [23]. Krt14 clearly stained the basal cells of the mammary duct with perfectly resolved Cd200 on some luminal cells lining inner of the basal ring (Fig. 3a-s, Supplementary Video 7). The relative distribution of Krt14 and Cd200 also show distinct patterns at specific micro-niche of the terminal end buds and ducts (Fig. 3t-y), suggests the spatial heterogeneity of the mammary cell composition and the benefit of observing tissue structures across distant locations at high spatial resolution.

We further explored the potential of using the microscope for pathological applications [24]. Human breast cancer tissue and the adjacent normal breast tissue were immuno-stained with Krt14 and Cd146 and cleared with Adipo-clear (Fig. 3z-gg, Supplementary Video 8). The cancer tissue lost its alveoli with abnormal tube structures and shows a denser vasculature system that likely favors the intravasation of cancer cells. The patient showed enlarged lymph nodes with suspicious metastatic cells that is consistent with our observation. The experiment suggests the prognostic value of cleared tissue imaging in pathological applications. Our microscope favors such a potential with its flexibility, reliability, and ease of use.

Evidently, we developed an advanced, versatile, and reliable tiling light sheet microscope to facilitate the application of cleared tissue imaging in different areas, the improvement of tissue fixation, clearing, and labeling methods, and the development of the

corresponding image analysis methods. Most importantly, it is made to be a regular tool for all scientists to take the benefits of cleared tissue imaging and discover its potential.

References

1. Micheva, K.D. & Smith, S.J. Neuron 55, 25-36 (2007).

2. Li, A., et al. Science 330, 1404-1408 (2010).

3. Ragan, et al. Nat. Methods 9, 255-258 (2012).

4. Moffitt, J.R., et al. Science, 362, aau5324 (2018).

5. Hama, H., et al. Nat. Neuroscience 14, 1481–1488 (2011).

6. Ertürk, A., et al, Nat. Protocols 7, 1983-1995 (2012).

7. Chung, K., et al. Nature 497, 332-337 (2013).

8. Susaki, E.A., et al. Cell 157, 726-739 (2014).

9. Pan, C., et al. Nat. Methods 13, 859-867 (2016).

10. Economo, M.N., et al. eLife 5, e10566 (2016).

11. Seiriki, K., et al. Neuron 94, 10185-1100 (2017).

12. Huisken, J., Swoger, J., Del Bene, F., Wittbrodt, J. & Stelzer, E.H.K. Science 305, 1007-1009 (2004).

13. Keller, P.J., Schmidt, A.D., Wittbrodt, J. & Stelzer, E.H.K. Science 322, 1065-1069 (2008).

14. Dodt, H.-U., et al. Nat. Methods 4, 331-336 (2007).

15. Tomer, R., et al. Nat. protocols 9, 1682-1697 (2014).

16. Dodt, H.-U., et al. Science 347, 474-475 (2015).

17. Tainaka, K., et al. Cell Report, 24 2196-2210 (2018).

18. Gao, R., et al. Science 363, eaau8302 (2019).

19. Fu, Q., Martin, B.L., Matus, D.Q., & Gao, L. Nat., Communcations 7, 11088 (2016).

20. Jing, D., et al. Cell Research 28, 803-818 (2018).

21. Li, W., Germaina, R.N. & Gernera, M.Y. Proc Natl Acad Sci U S A 114, E7321-E7330 (2017).

22. Tainaka, K., et al. Annu. Rev. Cell Dev. Biol. 32, 713–741 (2016).

23. Chi, J., et al. Cell Metabolism 27, 226-236 (2018).

24. Kubota, S.I., et al. Cell Reports 20, 236–250 (2017).

Acknowledgements

We thank Lorna Role and Benjamin L. Martin for providing the cleared Chat-Tau/EGFP mouse brain sample and zebrafish embryos. We thank Ming Yin, Yi Sun, Yalin Wang, Xufeng Wu, and John Hammer for helpful discussions. L.G., J.M.J., and S.C. acknowledge the support from the Westlake University.

Contributions

L.G. conceived the project and designed the microscope; L.G., J.M.J., and S.C. designed the experiments and supervised the research; L.G., X.L.L., M.L., and Y.W. constructed the microscope; L.G. and Y.W. developed the instrument control and data analysis software; D.Z., C.W., X.Z.L., R.F., Y.L.C., X.S.Z., X.Y., B.Z., Y.Y.C., Y.F., J.Y., and R.N. prepared the samples; X.L.L., M.L., W.Y., and L.G. performed the imaging experiments on the tiling light sheet microscope; D.D.Z, X.Z.L. performed the imaging experiments on the Zeiss Z1 light sheet microscope. L.G., J.M.J., S.C., X.L.L., M.L., Y.W., D.Z., C.W., X.Z.L., and B.C.C. analyzed the data; L.G., J.M.J., and S.C. wrote the paper with the input of all authors.

Competing interests

The authors declare no conflict of interest.

Figures

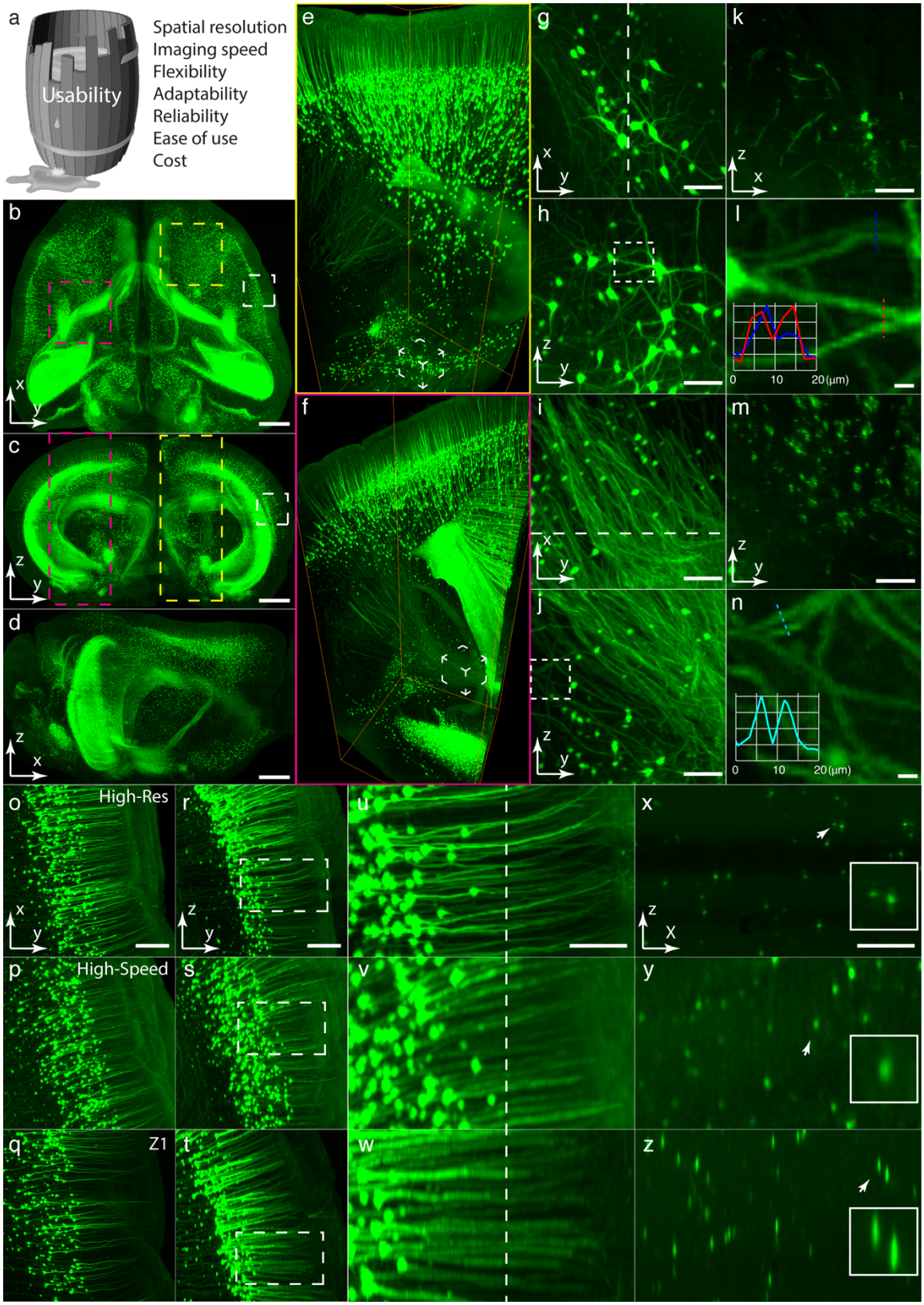
a
Usability
Spatial resolution
Imaging speed
Flexibility
Adaptability
Reliability
Ease of use
Cost
b
c
d
e
f
g
h
i
j
k
l
m
n
0
10
20 (μm)
o
High-Res
p
High-Speed
q
Z1
r
s
t
u
v
w
x
y
z

Figure 1. The design concept and characterization of the tiling light sheet microscope. (a) The microscope offers an advanced and versatile 3D imaging ability for cleared tissue imaging with emphases on multiple characters to make it widely applicable and easily adoptable. (b-d) xy, yz, and xz maximum intensity projections (MIP) of a cleared Thy1/YFP mouse brain imaged with our microscope. (e,f) 3D renderings of two selected 2 by 2 by 5 mm^3 regions in (b) and (c). (g-j) xy and yz MIPs of the selected regions in (e) and (f). (k,m) xz and yz image slices through the marked planes in (g) and (i). (l,n) Zoomed in views of the selected areas in (h) and (j). (o-t) xy and yz MIPs of the same 1 mm^3 cubic region, marked (white) in (b) and (c), imaged with a high resolution mode (o), a high speed mode (p) of our microscope, and a Zeiss Z1 light sheet microscope (q). (u-w) Zoomed in views of the selected areas in (r-t). (x-z) xz image slices through the marked planes in (u-w). All inserts are 50 by 50 μm^2, showing magnified views of the indicated dendrite cross sections. Scale bars, 1 mm (b-d), 100 µm (g-j,k,m,u,x), 10 µm (l,n), and 200 µm (o,r).

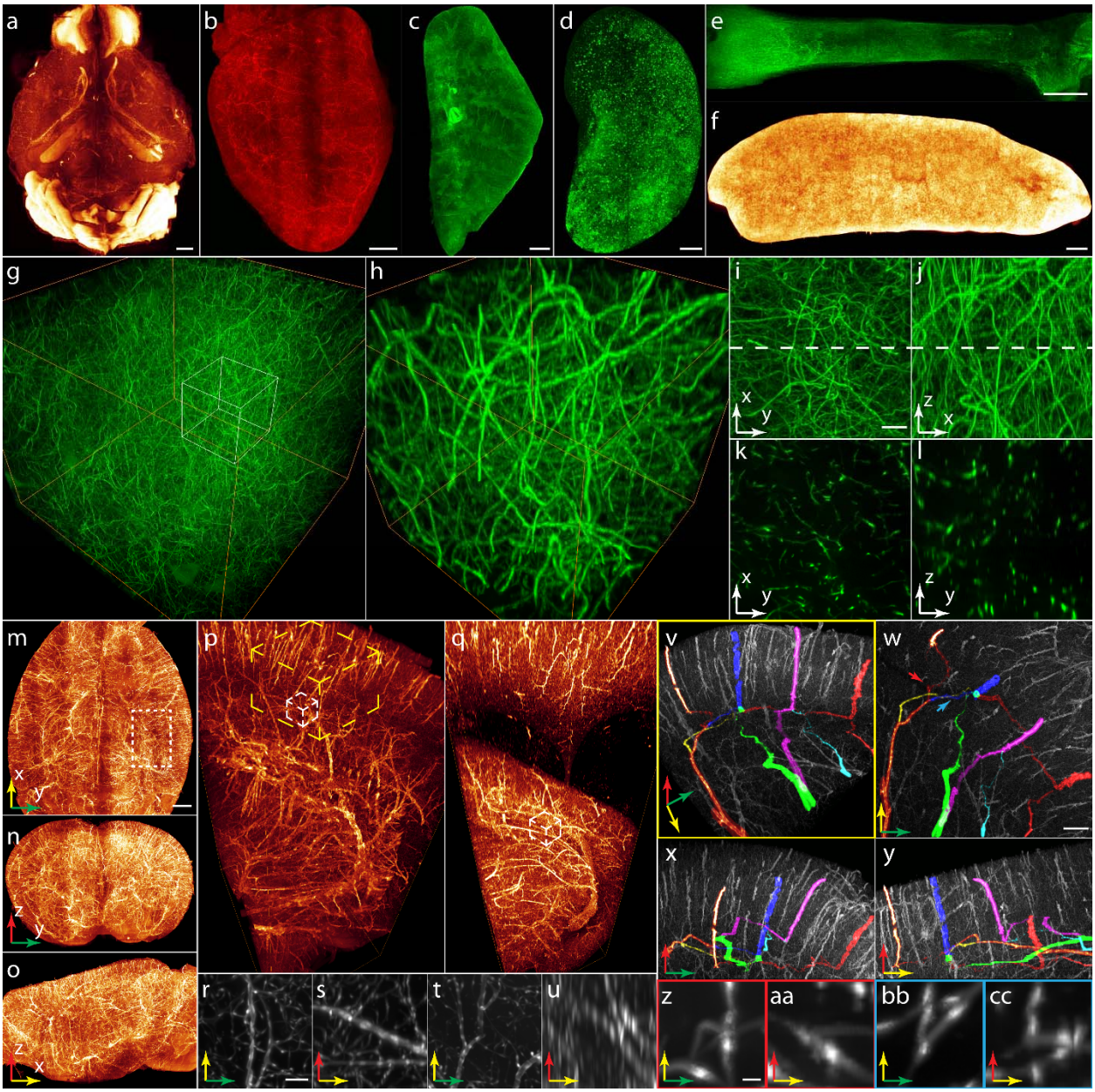
a
b
c
d
e
f
g
h
i
j
k
l
x
y
z
m
n
o
p
q
r
s
t
u
v
w
x
y
z
aa
bb
cc

Figure 2. The adaptability of the microscope. (a-f) 3D renderings of mouse brain, heart, lung, kidney, femur and spleen cleared with CUBIC (red) and PEGASOS (green), and imaged with our microscope. (g) 3D rendering of a 0.45 by 0.45 by 0.36 mm^3 region within a ~3 by 3 by 3 mm^3 mouse brain section, dissected from a CUBIC cleared Chat-Tau/EGFP mouse brain and imaged with a modified version of the presented microscope at a spatial resolution of ~0.5 by 0.5 by 3 μm^3. (h) Zoomed in view of the selected region in (g). (i,j) xy and xz MIPs of the same region in (h). (k,l) xy and yz image slices through the marked planes in (j) and (i). (m-o) xy, yz, and xz MIPs of a PEGASOS cleared SMACre-Ai14/tdTomato mouse brain labeling blood vessels. (p) 3D rendering of the selected region in (m). (q) 3D rendering of the same sample and region in (m) imaged with a Zeiss Z1 microscope. (r-u) xy and xz MIPs of the selected regions (white) in (p) and (q) showing the different spatial resolutions. (v) 3D rendering of the selected region (yellow) in (p) with multiple traces showing the connections between penetrating vessels and hippocampus vessels at corpus callosum via capillaries. (w-y) xy, yz, and xz MIPs of the region in (v). (z-cc) xy and xz MIPs of the red and blue arrows indicated locations in (w), showing the connecting capillaries. Scale bars, 1 mm (a-f, m), 20 µm (i), 40 µm (r), 200 µm (w) and 10 µm (z).

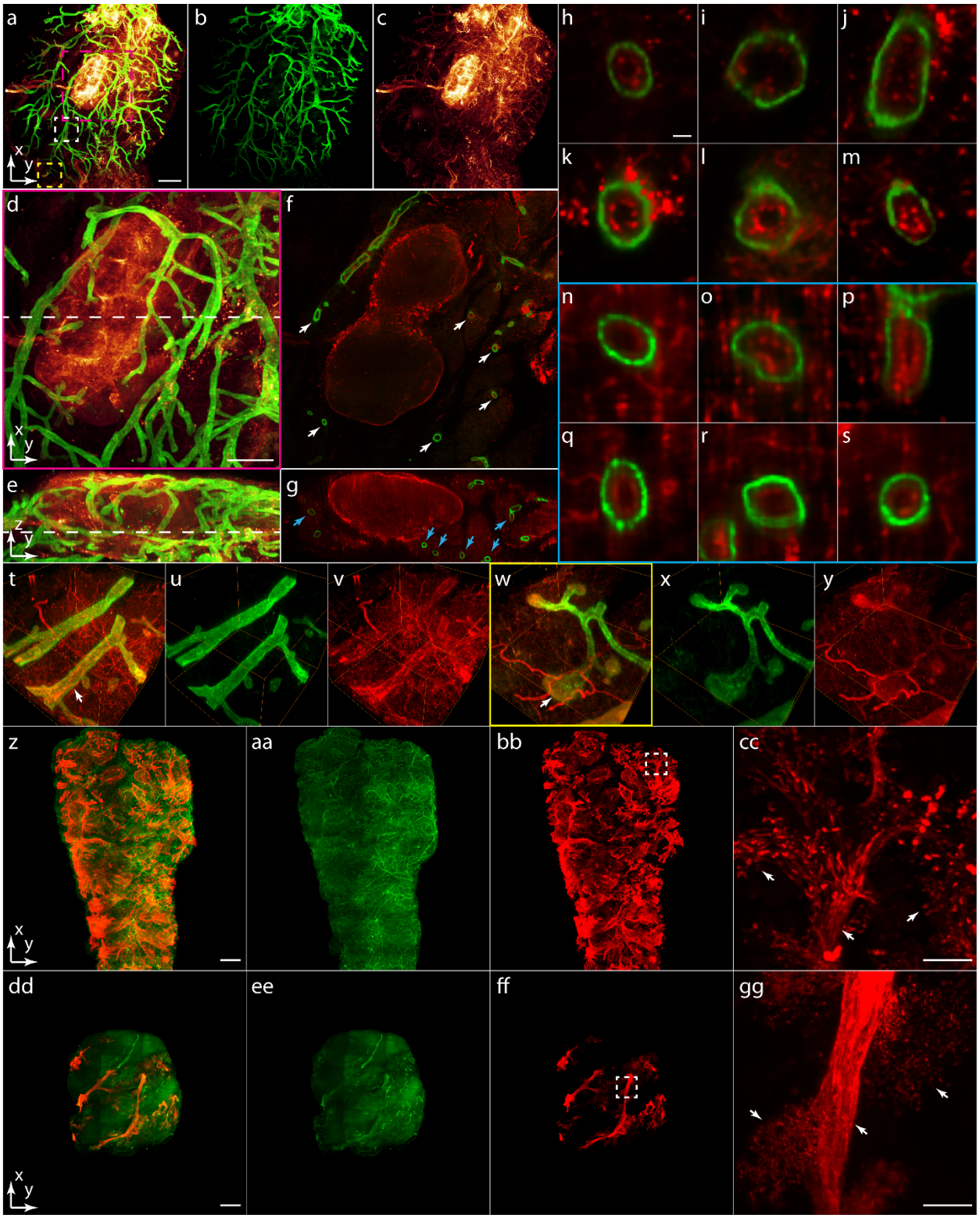
a
b
c
d
e
f
g
h
i
j
k
l
m
n
o
p
q
r
s
t
u
v
w
x
y
z
aa
bb
cc
dd
ee
ff
gg
x
y
z

Figure 3. The multicolor imaging ability of the microscope and its potential use for pathological applications. (a-c) 3D renderings of a cleared double color immuno-stained mouse mammary gland, rendered in both colors together and individually. (d-e) xy and yz MIPs of the selected (magenta) area in (a). (f-g) xy and yz image slices through the marked planes in (e) and (d). (h-s) Zoomed in views of the marked mammary duct lateral and axial cross sections in (f) and (g) showing the relative distribution of Krt14 and Cd200. (t-y) 3D renderings of two selected regions (white and yellow) in (a), showing distinct localization patterns of Krt14 and Cd200 at mammary ducts and end buds. (z-bb) 3D renderings of a cleared double color immuno-stained human breast cancer tissue. (cc) Zoomed in view of the selected area in (bb). (dd-ff) 3D renderings of a cleared double color immuno-stained normal human breast tissue adjacent to cancer tissue in (z). (gg) Zoomed in view of the selected area in (ff). The breast cancer tissue lost its alveoli and shows a much denser vasculature system. Scale bars 1 mm (a,z,dd), 500 µm (d), 20 µm (h), 200 µm (cc,gg).

Methods

Design considerations and microscope features

Cleared tissue imaging with LSM allows much easier access to high resolution tissue structure information than before. However, it is still challenging to implement the technique in many applications because conventional LSM has limited 3D imaging ability on large specimens [19] and conventional light sheet microscopes are not optimized to image cleared tissues. These microscopes usually have very limited 3D imaging ability on large cleared tissues and many practical restrictions on tissue clearing methods and mounting methods. They are often difficult to operate, too expensive and complicated for many research labs to acquire and maintain.

The wide application of cleared tissue imaging is also limited by several other issues. First, consistent and efficient tissue fixation and clearing methods that preserve tissue morphologies faithfully are necessary to ensure accurate visualization of tissue structures. However, most, if not all tissue fixation and clearing methods introduce tissue morphological distortions, which also could vary for different types of tissues. The influences of these methods to cellular morphology of different biological tissues need to be further investigated and evaluated.

Second, cleared tissue imaging has mainly been used to image transgenic mice organs due to the native fluorescent labels. Hence, the types of tissues and tissue structures could be imaged are limited. Tissue staining techniques that are capable to stain endogenous components in biological tissues of different species efficiently and uniformly are necessary to extend cleared tissue imaging to a much broader range of applications.

Third, the huge amount of data acquired in cleared tissue imaging turns into a burden quickly. Conventional microscopy data management and analysis workflow doesn't work in cleared tissue imaging. Solutions to manage, visualize, and analyze petabytes of 3D image data are needed urgently.

Finally, special optical components are required to improve the performance of light sheet microscopes designed for cleared tissue imaging. High resolution detection cameras, and long working distance, high numerical aperture (NA) objectives with large flatness corrected

detection field and refractive index correction for different imaging buffers are essential. Unfortunately, these components are rarely available, expensive, and often not optimized due to the lack of a significant supply and demand and the large variety of tissue clearing methods.

Therefore, a convenient, reliable, widely applicable, easily adoptable, and low cost microscope with advanced 3D imaging ability is critical to facilitate the application of cleared tissue imaging in different areas, enable active involvement of more scientists with different backgrounds to explore the potential of the technique, and have the problems discussed above solved. It could also stimulate the development and manufacture of optical components and devices optimized for cleared tissue imaging.

See the light, we developed a tiling light sheet microscope with more advanced 3D imaging ability for cleared tissue imaging. We also focused on improving the usability and decreasing the construction and operation cost of the microscope to make it easily adoptable. The microscope is uniquely characterized by the following features.

1. 3D Imaging ability and imaging speed: The microscope provides a more advanced 3D imaging ability and faster imaging speed than that of conventional light sheet microscopes. It is capable to image cleared biological tissue of centimeter sizes at micron level spatial resolutions within minutes to hours.

2. Flexibility: The 3D imaging ability of the microscope can be adjusted conveniently by changing the detection magnification and the excitation tiling light sheet, so that requirements for different spatial resolutions and imaging speeds in different applications can be satisfied.

3. Adaptability: The microscope is compatible with both aqueous and solvent based tissue clearing methods. Different sample mounting methods are used to mount samples of different sizes, shapes, and mechanical strengths so that the microscope can be used to image a large variety of biological tissues cleared and labeled with different methods. All subsystems of the microscope are independent, so that they can be modified to satisfy the requirements of applications beyond the ability of the current design.

4. Stability, reliability, and ease of use: The microscope solves most alignment problems by applying different binary phase maps to a SLM, which also enables semi-automatic alignment ability of the microscope. It makes the microscope extremely easy to operate and

ensures the delivery of the designed imaging ability in practice regardless the imaging conditions and user skills.

5. Minimum maintenance requirements: The microscope rarely requires maintenance due to the use of air objectives and the unique semi-automatic alignment ability. It reduces the microscope operation cost and increases its operation duty cycle at the same time.

6. Low cost: The construction cost of the microscope is roughly 105K USD with two 150 mW CW lasers. It could vary in different countries and regions. The operation cost is very low due to its excellent stability, ease of use, and minimum maintenance requirements.

7. Long life span: The microscope uses the latest tiling light sheet microscopy technique to achieve a more advanced 3D imaging ability. The independent subsystem design enables easy modification and upgrade to the microscope to improve its imaging ability and elongate its life span.

8. Availability: The complete microscope design, associated programs, and construct instruction can be obtained free for non-commercial use through the technique transfer office of the Westlake University.

Microscope configuration

The schematic diagram of the microscope and its configuration are shown in Supplementary Fig. 2. The combined laser beam with excitation wavelengths of 488 nm and 561 nm (Coherent OBIS 488 nm, 561 nm) is expanded to a $1/e^2$ beam diameter of ~7 mm (L1=30 mm, L2=250 mm) and sent to a binary spatial light modulator (SLM) assembly. The binary SLM assembly consists of a polarizing beam splitter cube, a half-wave plate and a 1280×1024 binary SLM for illumination light phase modulation. The modulated light is focused on an optical slit to block the undesired diffraction orders generated by the SLM and conjugated to a galvanometer mirror through relay lenses (L3=300 mm, L4=175 mm). The Galvo mirror is used to direct the illumination light to one of the two symmetrical illumination paths by offsetting the initial angle of the Galvo mirror and create a virtual excitation light sheet for sample illumination by scanning the laser beam. The laser beam is further conjugated to the real pupils of both excitation objectives through two pairs of relay lenses (L5=L7=150 mm,

L8=L9=250 mm) and illuminate the specimen from two opposite directions to minimize the excitation light traveling distance within the specimen. Both Mitutoyo MY5X-802 and MY5X-803 objectives can be used as the excitation objective in the current design. The two objectives have the same pupil size and working distance, while MY5X-803 has a 0.28 NA compared to the 0.14 NA of MY5X-802, so that a higher excitation NA, i.e. thinner light sheet, can be obtained by using MY5X-803.

The emitted fluorescence signal is collected with an Olympus MVX10 Macro Zoom microscope and imaged onto a sCMOS camera (Hamamatsu, Orca Flash 4.0) (Supplementary Fig. 2-3). A MVX10 microscope is used as the detection subsystem for several reasons. First, the microscope is equipped with multiple flatness corrected, long working distance objectives that are specifically designed to image large samples. Second, the microscope body is capable to adjust the magnification from 0.63× to 6.3×, so that the FOV size can be adjusted quickly for sample inspection and 3D imaging at the desired spatial resolution and imaging speed (Supplementary Fig. 5). Third, it has a conventional microscope design, so that the operation of the microscope is more convenient and familiar to most scientists. The MVX10 can be replaced by other similar Macro zoom microscopes, such as the Zeiss V16 microscope. The detection subsystem can also be as simple as a detection objective and a tube lens, whereas a more complicated design is required to allow the adjustment of the magnification conveniently.

The imaging chamber subsystem consists of an imaging chamber, a 3D sample translational stage, a buffer tray and a sample holder (Supplementary Fig. 2c-d). The sample is mounted on the sample holder driven by the 3D translational stage and immersed in the imaging buffer during imaging. The 3D translational stage can drive the sample for 26 mm in each dimension at a resolution of 8 nm. The imaging chamber is mounted on a waste buffer tray with a magmatic kinematic mount, so that it can be removed and replaced by a different imaging chamber containing different imaging buffer quickly, and the new chamber can be placed back to the same position accurately (Supplementary Fig. 3-4). The buffer tray is used as the mechanical reference of the imaging chamber and a container for spilled imaging buffers. All objectives are air objectives, which avoid the contamination caused by the imaging buffer.

Different sample mounting methods are used to mount samples of different sizes, shapes and mechanical strengths for 3D imaging. Two high pull magnets are used to attach the sample holder to the sample translational stage to enable quick and easy sample loading and unloading in seconds. Soft and stiff samples with more isotropic dimensions can be mounted with a clamp (Fig. 2a-b, Supplementary Fig. 4d-e) or be glued (Fig. 2c-e) on a steel spacer attached to the magnetic base of the sample holder (Supplementary Fig. 4f). Different spacers can be made via laser line cutting to fit samples of different shapes. Soft samples with a relative flat shape (Fig. 2f,3a,3z) can be pinned on the magnetic base of the sample holder with a couple of steel needles (Supplementary Fig. 4g). The excitation subsystem, detection subsystem and imaging chamber subsystem of the microscope are all independent, so that each subsystem can be modified individually to fit different applications when it is necessary (Fig. 2g, Supplementary Fig. 22-24).

Microscope control system

The microscope control system consists of a computer workstation, a NI PCIe-6323 DAQ card and a BNC 2090A connector block. The control system takes input parameters through the control software developed in Labview and generates the corresponding synchronized control signals to control the following opto-mechanical and opto-electrical devices of the microscope (Supplementary Fig. 5). A separate computer program assists the user to set up the imaging conditions and verify the alignment of the microscope.

1. Lasers: A 488 nm and a 561 nm laser are used to illuminate the specimen. The on/off status and the output power of each laser are controlled by an individual digital output (DO) signal.

2. Binary SLM: A binary SLM is used to generate tiling light sheets by applying different binary phase maps as described. Binary phase maps are loaded to the SLM via a USB interface. A DO signal synchronized with the scanning Galvo and the camera exposure is used to trigger the SLM.

3. Galvonometer: An analog DC voltage signal is used to control the Galvonometer. The Galvo has two functions. One is to scan the excitation laser beam to create a virtual light sheet,

the other is to direct the excitation laser beam to one of the two symmetrical excitation objectives by offsetting the initial angle of the Galvo mirror.

4. 3D translational stage: A 3D translational stage that consists of three identical Q522.230 linear stages is used to translate the sample in x, y (lateral) and z (axial) directions, and scan the sample in the axial direction for volumetric imaging. Each linear stage is controlled by an individual DO signal. Each linear stage moves one step at a preset step size for each TTL pulse received.

5. Filter wheel: A six position filter wheel is used for multicolor imaging. The filter wheel position is controlled by an individual DO signal.

6. Camera: The camera exposure is synchronized with the SLM and the Galvanometer with a DO signal. The collected images are captured and saved on the workstation through a camera link digital card.

Microscope imaging mode

The fundamental working principle of the microscope is similar to the tiling light sheet selective plane illumination microscope (TLS-SPIM) reported previously [19]. Specifically, the microscope works in four operation modes (Supplementary Fig. 6-7). 1. 2D imaging at a fixed image plane. 2. 3D imaging of a selected region of interest (ROI), in which the specimen is scanned in the axial direction using the z translational stage for 3D imaging. 3. 3D imaging of multiple selected ROIs, in which 3D imaging is performed at multiple selected lateral positions. 4. 3D imaging of an array of ROIs, in which 3D imaging is performed at an array of adjacent lateral positions to image a large sample volume. The details of each working mode are described below.

1. 2D imaging. The 2D imaging mode is mainly used for sample inspection. The camera acquires a given number of images or running continuously at a given exposure time. A tiling light sheet is tiled at different tiling positions by applying preloaded binary phase maps in sequence, which is synchronized with the camera exposure. The sample can be moved freely with the 3D translational stage during imaging. In each camera exposure period, the Galvo is scanned to create a virtual light sheet to illuminate the image plane through the selected

excitation objective (Supplementary Fig. 6b). A new phase map is applied to the SLM to tile the excitation light sheet based on the setting before every camera exposure. A raw image is collected at each tiling position. For multicolor imaging, the selected color channels alternate at each imaging plane after the excitation light sheet of the previous color channel finishes the tiling process at all tiling positions.

2. 3D imaging of a selected ROI. The microscope takes a 3D image stack of the selected ROI with the selected excitation objective in this mode, in which the sample is scanned in the axial direction with the z translational stage starting from the initial position at a given step size for a given number of steps (Supplementary Fig. 6c). At each image plane, the selected color channels fire in sequence to image the image plane using a tiling light sheet. The sample is scanned to the next axial position after the current image plane is imaged. The same imaging process repeats at all image planes until the entire 3D volume is imaged. The total number of raw images to be collected equals number of axial planes multiplied by the number of tiling positions and color channels. The imaging time equals the total number of raw images divided by the image frames per second. The raw data size equals the number of raw images multiplied by the data size of each raw image. The final data size equals the raw data size divided by the number of tiling positions.

3. 3D imaging of multiple selected ROIs. The microscope images multiple selected ROIs with the excitation objective assigned to each ROI (Supplementary Fig. 6c). The lateral positions and the axial scanning range of each ROI are recorded prior to the start of the imaging. A 3D image stack is taken for each selected ROI following the procedure described in the working mode 2. The 3D translational stage moves the specimen to the next ROI after the current ROI is imaged. The same 3D imaging process repeats until all selected ROIs are imaged.

4. 3D imaging of an array of adjacent ROIs. The microscope takes multiple 3D image stacks from an array of adjacent ROIs with the excitation objective assigned to each ROI to image a large sample volume. The microscope starts from the first ROI, takes a 3D image stack of the ROI as described in the working mode 2. The sample is translated to the next adjacent ROI, and the same 3D imaging process repeats to image the new ROI. The same process repeats until the entire array of ROIs are imaged. The ROIs are selected by setting the initial ROI lateral

position, the row and column numbers of the ROI array, and the lateral translation step size between the adjacent ROIs in x and y direction. A 10-15% overlap is usually maintained between adjacent ROIs for image registration of different ROIs.

Image analysis

The acquired image data are analyzed as follows (Supplementary Fig. 25).

1. The raw image data acquired from different ROIs are analyzed individually following the same procedure.

2. The raw images acquired in each ROI are separated to multiple 3D image stacks that are corresponding to different light sheet tiling positions. The number of separated 3D image stacks equals the number of tiling positions.

3. The region corresponding to the light sheet tiling position is determined for each separated 3D image stack, by which an amplitude mask is calculated for each separated image stack.

4. The 3D image of the ROI is obtained by summing the separated 3D image stacks multiplied by the corresponding amplitude mask determined in the previous step.

5. The same procedure is repeated to obtain the 3D image of all imaged ROIs. The amplitude masks obtained in the third step are usually same for all ROIs. They can also be adjusted for each individual ROI when necessary.

6. The 3D image of the entire sample volume is obtained by registering and merging the 3D image stacks of all ROIs using Amira. The final image data size is usually very large (hundreds of gigabytes to terabytes). The image reconstruction process could last from hours to days up to the data size and computational power. The obtained 3D image stacks of all ROIs could be down sampled first before being registered and merged to accelerate the image reconstruction for the whole sample volume.

7. Deconvolution is usually not applied due to the large data size. If necessary, the data were separated to smaller subvolumes and deconvolved using the Richardson-Lucy deconvolution algorithm in Matlab.

Troubleshooting

There are many common problems in cleared tissue imaging with LSM. Solutions to these problems with our light sheet microscope are described as follows.

1. Sample transparency. The transparency of the specimen is critical. Although many clearing methods have been developed, they behave differently on tissues of different types and sizes in our experiences. The clearing method needs be selected and optimized for the specific tissue. A simple method to evaluate if a sample is transparent enough is whether the sample could be seen through in imaging buffer by eyes.

2. Refractive index match. As described in Supplementary Fig. 15. It is very important to match the refractive indexes of the imaging buffer and the sample, which is also the fundamental principle of tissue clearing.

3. Different imaging buffers should never be mixed. Different imaging chamber should be used for different imaging buffers. The same imaging chamber should be cleaned and dried throughout before it is filled with a different imaging buffer.

4. Sample mounting. Due to the different sample sizes, shapes, mechanical strengths and chemical properties. The sample mounting method must be optimized for different samples. We developed several methods that could handle most types of cleared tissues in our experiences (Supplementary Fig. 4). Different sample mounting methods other than the described methods could be used to mount specimens can't be mounted with the current methods.

5. Sample handling. Cleared samples should be handled carefully in a clean environment during sample mounting. Sample exposure in air should be avoided as much as possible. Any dust, non-imaging buffer droplet, glue, etc. attached to the sample surface or air bubble trapped in the sample could degrade the imaging quality.

6. Imaging buffer handling. The imaging buffer should be handled gently to avoid generating air bubbles in the imaging buffer. Any inconsistency of the imaging buffer could degrade the imaging quality.

7. Imaging buffer evaporation. Due to the open top imaging chamber design in our microscope. Imaging buffer evaporation could cause slow refractive index variation of some imaging buffer in imaging experiments last for many hours. The problems can be minimized by:

1. Using the focus correction method described in Supplementary Fig. 8-9 to corrected the light sheet axial position. 2. Changing the imaging buffer routinely every few hours. 3. Floating a thin cover slip on the imaging buffer surface to reduce imaging buffer evaporation. Again, since the image chamber subsystem is independent, a sealed imaging chamber could be used for imaging buffer that evaporates too fast.

8. Toxic imaging buffers. The vapor of some imaging buffers could be toxic. The microscope could be placed in an enclosure with exhaust fans to solve the problem.

9. Microscope misalignment. We describe all alignment problems and the corresponding solutions in Supplementary Fig. 8, 9, 15. All alignment problems and drifts are corrected with the spatial light modulator by applying different phase maps. Users are assisted by the control program to generate the binary phase maps and confirm the imaging quality during microscope calibration. Hardware alignment or maintenance is rarely needed for our microscope after the initial construction.

10. Tiling position drift. The tiling light sheet positions could drift due to the inconsistent refractive index of the cleared tissue or a slight mismatch between the refractive indexes of the imaging buffer and the sample. Such a drift can be corrected by shifting the amplitude mask position described in image analysis step 3.

Sample preparation

Sample cleared with different methods are prepared as follows.

CUBIC

Mice were deeply anesthetized using pentobarbital (~150 mg/kg of body weight; i.p.) and perfused with heparinized 0.1 M PBS (10 U/ml of Heparin) for 5-10 minutes at room temperature until the blood was washed out, followed by 4% paraformaldehyde (PFA) in 0.1 M PBS (pH 7.4). Subsequently, organs from these animals were dissected out and post-fixed in 4% PFA overnight at 4°C, washed with 0.1 M PBS for 2 hours twice at room temperature and delipidated with CUBIC reagent 1 (25 wt% urea, 25 wt% Quadrol and 15 wt% Triton X-100). PI (5 µg/ml) was added to reagent 1 for nuclear stained specimens. Replace the reagent every 2 days untill organs were sufficiently cleared. After delipidation, organs were washed with PBS for 2

hours three times at room temperature with gentle shaking, and then immersed in CUBIC-2 (25 wt% urea, 50 wt% sucrose and 10 wt% triethanolamine) at 37 °C with gentle shaking overnight. The reagent was replaced with fresh reagent afterwards and organs were further incubated until transparent.

PEGASOS

Dissected mouse tissues and bones were immersed in 5 ml of 4% paraformaldehyde (PFA) on a roller-mixer at room temperature for 24 hours and washed in PBS three times afterwards. Bones were decalcified next in 20% Ethylenediaminetetraacetic acid(EDTA) for 4 days, while soft tissues were directly immersed in 25% N,N,N′,N′-Tetrakis (2-Hydroxypropylethylenediamine; Quadrol) water solution for 2 days and 5% ammonium solutions for 1 day in sequence for decolorization. Samples were immersed in tert-butanol (tB) solutions with gradient concentrations of 30% v/v, 50% v/v, and 70% v/v, for 1 to 2 days for delipidation, then dehydrated with 70% tB v/v, 27% polyethylene glycol (PEG) v/v, 3% Quadrol v/v for 2 days. Samples were finally cleared in BB-PEG medium composed of 75% benzyl benzoate (BB), 22% PEG, and 3% Quadrol for 2 days. Cleared tissues were preserved in BB-PEG at room temperature after clearing.

Adipo-Clear

The immunostaining and clearing of the mouse mammary gland, human breast cancer and paracancerous tissues (Approved by the independent ethics committee of Zhejiang cancer hospital (approval No: IRB-2015-176)) were conducted with a modified Adipo-Clear method. Briefly, the tissues were fixed with 4% PFA overnight, permeabilized with 1% Triton-X100-PBS for 1day, incubated with primary and then secondary antibodies in 37℃ for 4 days respectively. Rabbit anti-keratin 14 (Biolegend, Poly19053, 1:500), rat anti-CD200 (Biolegend, 123802, 1:200) or mouse anti-CD146 (ebioscience, 11-1469-41, 1:100) were used as primary antibodies. Alexa Fluor 488 or 594 conjugated donkey IgGs (Jackson) are used as secondary antibodies. After immunostaining, the tissues are dehydrated through 25%, 50%, 75% and 100% methanol, then

delipidated with dichloromethane (DCM, sigma, 270997) and finally incubated in dibenzyl ether (DBE, sigma, 108014) before imaging.

Zebrafish embryos

Nuclei of zebrafish embryos were labelled by ubiquitous expression of nuclear localized Kikume green/red photoconvertible protein (NLS-KikGR). Membrane of zebrafish embryos were labeled by membrane-targeted GFP injection.